Journal of Materials Chemistry C

Increased charge carrier mobility and molecular packing of a solution sheared diketopyrrolopyrrole-based donor-acceptor copolymer by alkyl side chain modification

Journal:	*Journal of Materials Chemistry C*
Manuscript ID	TC-ART-12-2018-006255.R1
Article Type:	Paper
Date Submitted by the Author:	21-Feb-2019
Complete List of Authors:	Hambsch, Mike; Technische Universitat Dresden, Center for Advancing Electronics Dresden Erdmann, Tim; Leibniz-Institut für Polymerforschung Dresden e.V., Polymer Structures Chew, Annabel; Stanford University Bernstorff, Sigrid; Elettra - Sincrotrone Trieste S.C.p.A., Salleo, Alberto; Stanford University Kiriy, Anton; Leibniz Institute of Polymer Research Dresden, Nanostructured Materials Voit, Brigitte; Leibniz Institute of Polymer Research Dresden, Mannsfeld, Stefan; Technische Universität Dresden,

Increased charge carrier mobility and molecular packing of a solution sheared diketopyrrolopyrrole-based donor-acceptor copolymer by alkyl side chain modification

Mike Hambsch[1,2*], Tim Erdmann[1,3#], Annabel R. Chew[4], Sigrid Bernstorff[5], Alberto Salleo[4], Anton Kiriy[1,3], Brigitte Voit[1,3], Stefan C.B. Mannsfeld[1,2*]

[1] Center for Advancing Electronics Dresden, Technische Universität Dresden, 01062 Dresden, Germany

[2] Faculty of Electrical and Computer Engineering, Technische Universität Dresden, 01062 Dresden, Germany

[3] Leibniz-Institut für Polymerforschung Dresden e.V., 01069 Dresden, Germany

[4] Department of Materials Science and Engineering, Stanford University, Stanford, CA 94305, USA

[5] Elettra-Sincrotrone Trieste, 34149 Basovizza, Italy

[#] Present address: IBM Almaden Research Center, 650 Harry Road, San Jose, CA 95120, USA.

*email: mike.hambsch@tu-dresden.de, stefan.mannsfeld@tu-dresden.de

Keywords: organic semiconductors, organic field-effect transistors, solution shearing, charge modulation spectroscopy

Abstract

Semiconducting polymers based on diketopyrrolopyrrole have achieved high charge carrier mobilities in field-effect transistors due to their strong intermolecular interactions, which lead

to a high structural order that is beneficial for charge transport. One factor that influences the degree of order in thin films is the choice of solubilizing side chains. In this study, we present a new polymer, poly{3-([2,2':5',2''-terthiophen]-5-yl)-2,5-bis(6-dodecyloctadecyl)-2,5-dihydropyrrolo[3,4-c]pyrrole-1,4-dione-6,5''-diyl}, which has extended side chains and side-chain branching points that were moved further away from the polymer backbone. Bottom-gate, top-contact field-effect transistors from solution sheared films of this material show average saturation hole mobilities of close to 1 cm^2/Vs which is higher than in devices of a commonly used version of this polymer with shorter side chains. The increase in mobility is attributed to an improved structural order in the thin-film state and a decrease in π-π stacking distance. The fabricated devices show very good air-stability without significant degradation in performance after more than one year storage under ambient conditions.

Introduction

Donor-acceptor copolymers based on the electron-accepting diketopyrrolopyrrole (DPP) in combination with electron-donating moieties, most commonly thiophene, have been the subject of extended research for organic field-effect transistors (OFETs),[1–7] solar cells (OPVs)[8–11] and photodetectors (OPDs)[12,13] in the last few years. Their propensity to form strong intermolecular interactions and a high degree of chain coplanarity, often resulting in a high structural order and densely packed thin films, makes them an interesting material for organic electronics.[1,14] OFETs based on DPP in particular have garnered great interest for achieving charge carrier mobilities which are amongst the highest for polymer semiconductors, with values of up to 13 cm^2/Vs depending on the composition of donor and acceptor groups of the polymers.[1,6,7,15,16]

One way to further optimize the order and packing in the solid state for efficient charge transport in OFETs is the modification of the solubilizing side chains. Lee et al. investigated the influence of the alkyl chain length (2-octyldodecyl vs. 2-hexyldecyl) on the transistor performance of two DPP-based polymers.[17] The difference in the molecular structure was the

electron-donating group either being terthiophene or thiophene-thieno[3,2-*b*]thiophene-thiophene. For both polymers they observed the same trend: by extending the alkyl chains, the structural order in the films increased, resulting in higher charge carrier mobilities. The same trend has also been observed for copolymers consisting of DPP as electron-accepting moiety and a π-extended thiophene unit [(*E*)-2-(2-(thiophen-2-yl)vinyl)thiophene] as electron-donating group. The polymer with the longer side chains, 2-decyltetradecyl in comparison to 2-octyldodecyl achieved higher carrier mobilities due to a smaller π-π stacking distance.[18]

Besides the length of the alkyl chains, the position of the branching point has also an influence on the film structure and packing. Karpov et al. have shown that by extending the solubilizing side chains and moving the branching point further away from the backbone (6th carbon instead of 2nd carbon) of a copolymer consisting of DPP and thienothiophene-thiophene, the crystallinity and molecular packing is improved resulting in a higher charge carrier mobility in field-effect transistors.[19]

Here, we present a new DPP-based polymer poly{3-([2,2':5',2''-terthiophen]-5-yl)-2,5-bis(6-dodecyloctadecyl)-2,5-dihydropyrrolo[3,4-c]pyrrole-1,4-dione-6,5''-diyl} (P(DPP6DOT2-T)) with solubilizing side chains that have been extended and a branching point that has been moved further away from the backbone in comparison to the previously reported poly{3-([2,2':5',2''-terthiophen]-5-yl)-2,5-bis(2-octyldodecyl)-2,5-dihydropyrrolo[3,4-c]pyrrole-1,4-dione-6,5''-diyl} [P(DPP2ODT2-T)].[14,17,20–22] Depending on the device architecture and the utilized fabrication process, OFETs with P(DPP2ODT2-T) have shown hole mobilities in the range of 0.04 – 2.4 cm^2/Vs. Here, we prepared bottom-gate top-contact field-effect transistors with both polymers utilizing solution shearing as deposition technique. This processing technique has been shown to achieve much higher charge carrier mobilities for some small molecule semiconductors than devices fabricated by spin coating, which has been attributed to the method's ability to tune the film morphology and to stabilize polymorphs that are favorable for charge transport.[23–25] In recent years, researchers have also begun to apply solution shearing to semiconducting polymers and achieved an improved transistor

performance based on changes in the film microstructure and a possible alignment of the polymer chains.[26–28]

In this work, devices, which were fabricated using the polymer with the extended side chains showed more than three times higher saturation hole mobilities ($\mu_{sat,avg}$ = 0.7 cm^2/Vs) than the ones with the standard side chains ($\mu_{sat,max}$ = 0.2 cm^2/Vs). We attribute this increase in mobility to a more preferential packing of the polymer (decreased π-π stacking distance and higher relative fraction of crystalline domains) as evidenced by grazing incidence wide angle X-ray scattering (GIWAXS). The devices also show a high degree of air stability, maintaining around 83% of the initial mobility after more than one-year storage under ambient conditions.

Results and discussion

Material synthesis and characterization

The two DPP-based semiconducting polymers investigated in this study, P(DPP2ODT2-T) and P(DPP6DOT2-T) (**Fig. 1**), were synthesized by palladium catalyzed Stille coupling polycondensation using the respective co-monomers (**Fig. S1**) and literature procedures.[14,19] The number average molecular weight (M_n) and dispersity ($Đ = M_w/M_n$) of the copolymers were analyzed by gel permeation chromatography (GPC) at 40 °C and high-temperature GPC (HT-GPC) at 150 °C using chloroform and 1,2,4-trichlorobenzene as solvent, respectively (**Table 1**). While the molecular weights obtained by HT-GPC are comparable (M_n = 16.8 kg/mol vs. 19.4 kg/mol for P(DPP2ODT2-T) and P(DPP6DOT2-T), respectively), the ones derived from GPC differ significantly (M_n = 54.1 kg/mol vs. 160.5 kg/mol for P(DPP2ODT2-T) and P(DPP6DOT2-T), respectively). For both polymers, GPC curves revealed a bimodal molecular weight distribution assigned to be caused by strong aggregation (**Fig. S12**). While HT-GPC conditions were able to break up high molecular-weight aggregates in P(DPP2ODT2-T), aggregation is still indicated for P(DPP6DOT2-T) by the formation of a shoulder in the HT-GPC curve. This points to stronger aggregation and intermolecular interactions in P(DPP6DOT2-T),

enabled by shifting the branching point in the side chains further away from the polymer backbone.

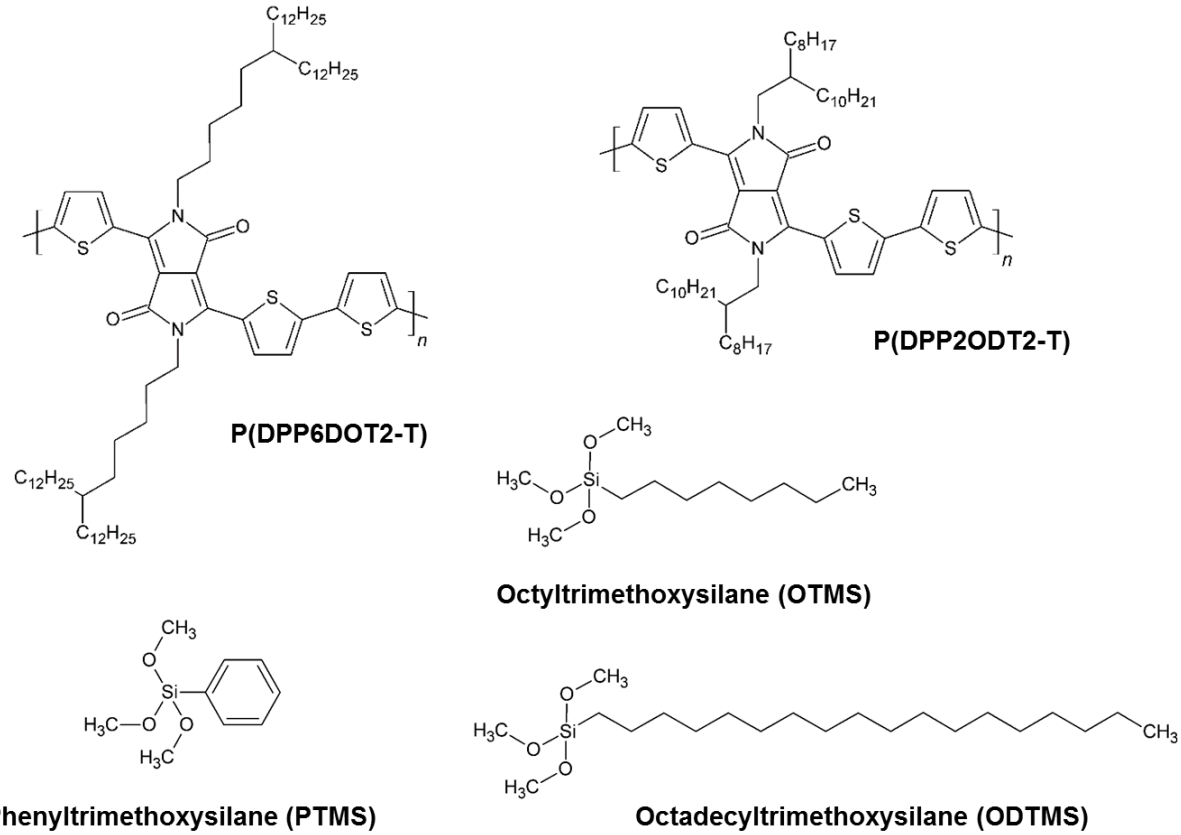

Fig. 1 *Chemical structure of the two studied diketopyrrolopyrrole polymers and the different silanes used as interfacial layers in bottom gate top contact field-effect devices.*

Table 1 *Physicochemical properties of P(DPP2ODT2-T) and P(DPP6DOT2-T).*

	GPC[a] M_n [kg/mol]	Đ	HT-GPC[b] M_n [kg/mol]	Đ	E_g [eV][c]	E_{HOMO} [eV][d]	E_{LUMO} [eV][e]
P(DPP2ODT2-T)	54.1	4.1	16.8	2.3	1.34	-5.60	-4.26
P(DPP6DOT2-T)	160.5	2.4	19.4	2.5	1.31	-5.55	-4.24

[a] In $CHCl_3$ at 40 °C. [a,b] Based on a calibration with PS standards. [b] In 1,2,4-trichlorobenzene at 150 °C. [c] Determined using the onset wavelength of the absorption edge in thin-film UV-Vis spectra. [d] Calculated by $E_{HOMO} = -(5.09 + E_{onset,ox\ vs.\ Fc/Fc+})$ [eV]. [e] $E_{LUMO} = E_g + E_{HOMO}$.

The thermal properties were investigated by thermogravimetric analysis (TGA) and differential scanning calorimetry (DSC). P(DPP6DOT2-T) and P(DPP2ODT2-T) showed good thermal stability with decomposition temperatures of 416 °C and 407 °C, respectively (**Fig. S2**). In DSC measurements, P(DPP6DOT2-T) and P(DPP2ODT2-T) demonstrated an endothermic phase

transition during the heating scan at a peak temperature of 349 °C and 270 °C, respectively, which was assigned to the melting of the polymer backbone (**Fig. S3**). An exothermic phase transition during the cooling scan was observed at a peak temperature of 346 °C and 263 °C, respectively, indicating the crystallization of the polymer backbone (**Fig. S3**). The large difference in melting and crystallization peak temperatures between the two polymers (ΔT = 79 K and 83 K, respectively) cannot be solely explained by the increase in mass of the repeating unit and, thus, points to stronger intermolecular interactions in P(DPP6DOT2-T). More detailed information can be found in the supporting information section on the thermal properties of the polymers (**Table S3, Fig. S4 and S5**). The optoelectronic properties of the copolymer thin films were studied by UV-Vis absorption spectroscopy and cyclic voltammetry (CV). The UV-Vis spectra present two spectral features, a high-energy π-π* transition band at ~413 nm and a low-energy intramolecular charge-transfer (CT) transition band at ~842 nm and ~828 nm for P(DPP6DOT2-T) and P(DPP2ODT2-T), respectively (**Fig. S6**). In addition, both spectra show a shoulder of the CT band to higher energies at ~770 nm. Besides the shift of the absorption maximum by +14 nm in P(DPP6DOT2-T) thin-films, the CT transition band is also slightly expanded to higher and lower energies, representing a wider variety of optical transitions possibly caused by enhanced intermolecular interactions. The optical band gap energies were determined from the onset wavelength of the absorption edge and are almost not affected by the different side-chain architectures (**Table 1** and **S1**). In CV scans, an irreversible oxidation was observed for P(DPP6DOT2-T) and P(DPP2ODT2-T) as can be seen in **Fig. S7**. From the onset potential of the oxidation the energy of the highest occupied molecular orbital (HOMO) of -5.55 eV and -5.60 eV was determined, respectively (**Table 1**). By taking the optical gap energies into account, the respective energy of the lowest occupied molecular orbital (LUMO) was calculated to -4.24 eV for P(DPP6DOT2-T) and -4.26 eV for P(DPP2ODT2-T). Thus, the structural side-chain modifications resulted in only minor changes of the optoelectronic properties.

Solution sheared devices with different SAMs

The electronic properties of the new polymer were evaluated in bottom-gate, top-contact field-effect transistors (**Fig. 2a**). To achieve an optimized device performance, we compared different self-assembled monolayers (SAMs) that are commonly used to chemically modify the SiO_2 dielectric in OFETs.[2,29] The chemical structures of the SAMs, namely phenyltrimethoxysilane (PTMS), octyltrimethoxysilane (OTMS), and octadecyltrimethoxysilane (ODTMS) are shown in **Fig. 1**. Films of P(DPP6DOT2-T) were then deposited on top of the SAM-treated substrates by solution shearing (**Fig. 2b**) using different shearing speeds. The maximum attainable shearing speed was found to be limited by the wetting behavior of the semiconductor solution on top of the hydrophobic ODTMS – in our case 0.5 mm/s. For the tested range of speeds from 0.1 – 0.5 mm/s, a clear trend for all the various SAMs was observed with mobility decreasing with increasing speed (**Fig. S8**). If not stated otherwise, a shearing speed of 0.1 mm/s has therefore been used for all samples in the following experiments.

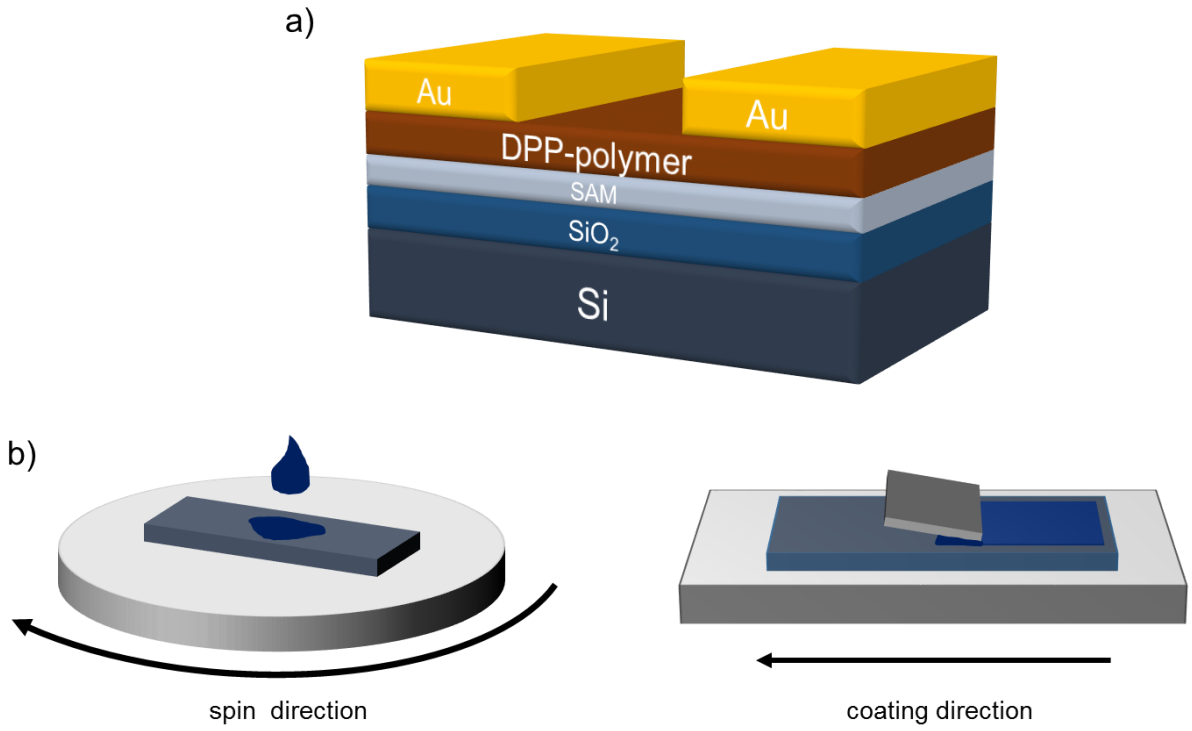

Fig. 2 *a) Device architecture of the bottom-gate top-contact field-effect transistors. Schematic of b) the spin coating process and c) the solution shearing process.*

The devices prepared without SAM or with SAMs of PTMS and OTMS all show similar transistor characteristics. Only the devices with ODTMS SAMs exhibit significantly different device characteristics. **Fig. 3a** shows the transfer characteristics of representative devices with the different SAMs and clearly demonstrates that the ODTMS devices have an increased on- and off-current as well as a V_{on} that is strongly shifted towards more positive voltages. When plotting $I_d^{1/2}$ for extracting the threshold voltage and saturation charge carrier mobility, we observe a non-linear slope or "kink" in the curve (**Fig. 3b**), meaning the extracted mobility values depend on the applied gate voltage as illustrated in **Fig. S9**. This effect has been intensely discussed in the recent literature[30–34] because of the potential overestimation of charge carrier mobilities in the past in many publications. The current consensus is that the origin of this effect is a gate voltage-dependent contact resistance, caused by non-ohmic injection from the electrode into the semiconductor. The recent discussions about this potential overestimation of the carrier mobility in devices with non-ideal transfer characteristics is slowly leading to a more careful and conservative way of reporting mobility values.

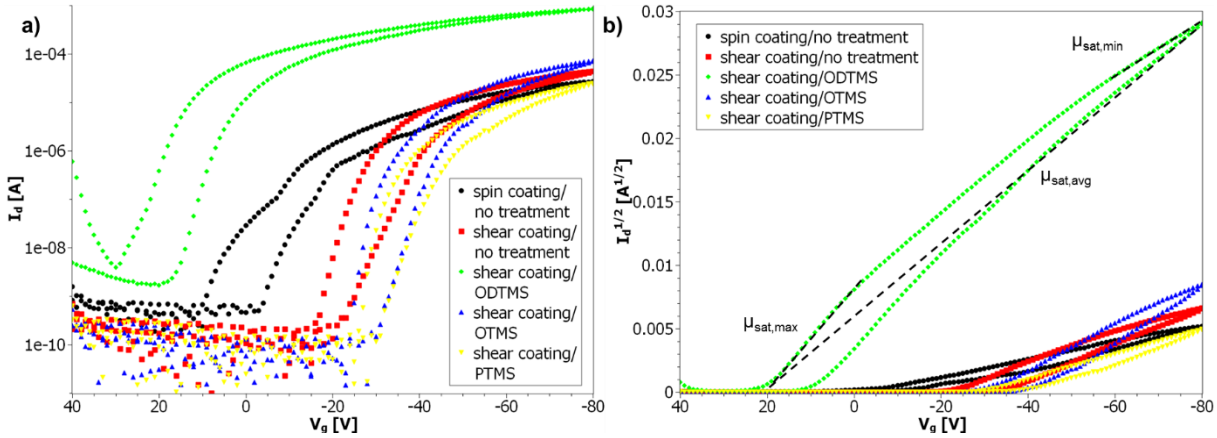

Fig. 3 *a) Transfer characteristics of typical field-effect transistors prepared either by spin coating or solution shearing with different surface modifications (V_{ds} = -80 V). b) Square root plot of the transfer characteristics (V_{ds} = -80 V) used for calculating the saturation mobility. The black lines indicate the different gate voltage dependent mobility regimes. $\mu_{sat,max}$ represents the mobility at gate voltages close to the threshold voltage, $\mu_{sat,min}$ represents the mobility at high gate voltages and $\mu_{sat,avg}$ the averaged mobility between the threshold voltage and the maximum applied gate voltage.*

In our work, we will report both the maximum saturation mobility ($\mu_{sat,max}$) extracted from the slope close to the threshold voltage and the minimum saturation mobility ($\mu_{sat,min}$) at high gate

voltages as shown in **Fig. 3b**. This approach has been recently adopted by other research groups as well.[35–37] Additionally, we will also calculate the average saturation mobility ($\mu_{sat,avg}$), which is the mobility value based on the average slope in the $I_d^{1/2}$ plot between the threshold voltage and the maximum applied gate voltage. We believe this to be the most transparent way of reporting effective mobility values, which can be compared to other reports in the literature. It is also important to remember that these field-effect mobilities from devices might not represent the materials intrinsic mobility. The transistor parameters of the different solution sheared devices and reference transistors with a spin coated semiconductor layer are summarized in **Table 2**. There it can be seen that for the devices prepared on the ODTMS treated SiO_2 the difference between $\mu_{sat,max}$ and $\mu_{sat,min}$ is the most pronounced ($\mu_{sat,max}$ = 1.1 cm^2/Vs and $\mu_{sat,min}$ = 0.3 cm^2/Vs). For the devices on other SAMs or untreated SiO_2 the difference between the two mobility regimes is smaller but the overall mobility values are also lower. We also observe a more than 50 V shift of the threshold voltage to more positive voltages for the ODTMS-based transistors. This effect has been investigated in the literature before and is often attributed to the introduction of additional charge carriers in the semiconductor due to the molecular dipoles of the ODTMS.[38,39]

Table 2 *Parameters of the different P(DPP6DOT2-T) field-effect transistors prepared by either spin coating or solution shearing with various silane-based SAMs.*

Process	**Spin coating**	**Solution shearing**			
Surface	SiO_2	SiO_2	ODTMS	OTMS	PTMS
V_{th} [V]	-3 ± 3	-22 ± 2	20 ± 2	-31 ± 5	-31 ± 5
$\mu_{sat,avg}$ [cm^2/Vs]	0.02 ± 0.003	0.09 ± 0.03	0.57 ± 0.04	0.17 ± 0.09	0.10 ± 0.05
$\mu_{sat,min}$ [cm^2/Vs]	0.01 ± 0.002	0.05 ± 0.01	0.32 ± 0.01	0.12 ± 0.05	0.07 ± 0.02
$\mu_{sat,max}$ [cm^2/Vs]	0.02 ± 0.004	0.13 ± 0.05	1.06 ± 0.06	0.22 ± 0.12	0.12 ± 0.07
I_{on}/I_{off}	$3x10^4 \pm 2x10^4$	$2x10^6 \pm 1x10^6$	$2x10^5 \pm 7x10^4$	$4x10^7 \pm 4x10^7$	$6x10^7 \pm 5x10^7$

$\mu_{sat,avg}$ are the average saturation mobilities between the threshold voltage and the maximum applied gate voltage. $\mu_{sat,min}$ are the saturation mobilities at high gate voltages (between -60 and -80 V) and $\mu_{sat,max}$ are the ones close to the threshold voltage (between V_{th} and V_{th} – 20 V). See Figure 3b for better understanding. All numbers are averages and standard deviations of at least six devices measured in forward direction.

For a better understanding of the differences in charge carrier mobility between devices having an ODTMS SAM and devices without SAM treatment we performed charge modulation spectroscopy (CMS)[40–42] on the different semiconductor films. CMS allows the polaron absorption of semiconductors in metal-insulator-semiconductor (MIS) devices to be directly measured by modulating the field-induced charges under operating conditions that are comparable to OFETs. This is done through modulation of the gate voltage in the MIS device, which controls the charge density at the dielectric/semiconductor interface. By measuring in-situ the changes in the transmission spectra of the MIS devices at different applied gate voltages (e.g. in accumulation and depletion), the change in absorption (ΔT/T) solely due to polarons present in the device can be extracted, assuming hopping transport of carriers between localized states due to the strong electron-phonon coupling in organic semiconductors.[43] As a result, the CMS measurement captures information about the degree of delocalization of the charges directly involved in charge transport in OFETs.[44,45]

Fig. 4 shows the charge modulation spectra of solution sheared P(DPP6DOT2-T) on SiO_2 with and without ODTMS SAM. From the spectra it can be seen that the overall polaron absorption intensity of the film with ODTMS SAM is significantly higher than of the one without it. This suggests a higher degree of polaron delocalization,[45] most likely due to an increase in local chain ordering resulting in a higher charge carrier mobility, as observed in this work. This finding is in good agreement with CMS measurements of spin-coated poly(3-hexylthiophen-2,5-diyl) (P3HT) films, where the use of an octadecyltrichlorosilane SAM led to an increase in polaron size by more than a factor of two.[46] Chew et al. attributed this increase in polaron delocalization and consequently charge carrier mobility to an improved polaron coherence originating from a reduced energetic and conformational disorder at the SAM/P3HT interface and not just an increased degree of crystallinity. For a quantitative analysis of the charge

modulation spectra of P(DPP6DOT2-T), including the calculation of polaron coherence lengths, a complete theoretical model similar to the one that has been derived for P3HT is necessary, and currently under development.

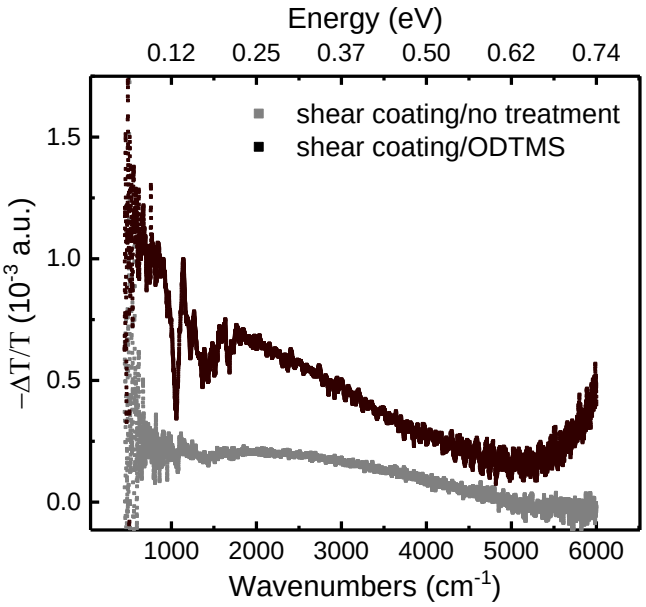

Fig. 4 *Charge modulation spectra of solution sheared P(DPP6DOT2-T) prepared on substrates with (black) and without (gray) ODTMS SAM.*

Influence of the solubilizing side chain structure on film structure and transistor performance

After finding the optimized fabrication conditions (ODTMS SAM and shearing speed of 0.1 mm/s) for devices with solution sheared P(DPP6DOT2-T), we prepared transistors with P(DPP2ODT2-T) under the same conditions to directly compare what influence the changes to the side chains have on the electrical performance. The transfer characteristics of typical devices with the two polymers are shown in **Fig. 5**. Both semiconductors have a similar threshold voltage but P(DPP6DOT2-T) exhibits much higher on-currents and therefore a higher mobility ($\mu_{sat,avg}$ = 0.7 cm^2/Vs compared to 0.2 cm^2/Vs). The mobility values for the P(DPP2ODT2-T) devices are of the same order of magnitude to what was reported in the literature for devices prepared by spin coating with either bottom- or top-gate architecture, although the previously mentioned uncertainty in reported mobility values needs to be considered.[14,21,47] The transistor parameters are summarized in **Table 3** and show that the

extension of the side chains led to an increase in saturation mobility by a factor of around 3, independently of what gate voltage range is used for the extraction of the mobility values.

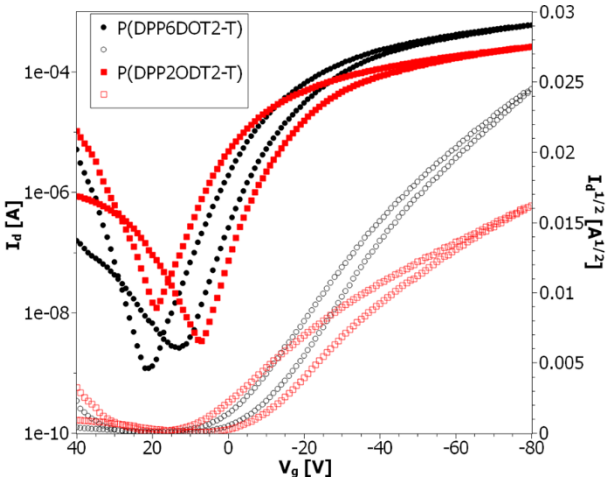

Fig. 5 *Comparison of the transfer characteristics of solution sheared P(DPP6DOT2-T) and P(DPP2ODT2-T) transistors with identical device geometry and processing conditions. It can be seen that P(DPP6DOT2-T), the polymer with the extended side chains shows an improved mobility.*

Table 3 *Comparison of the parameters of transistors with solution sheared films of P(DPP6DOT2-T) and P(DPP2ODT2-T) using ODTMS.*

Polymer	**P(DPP6DOT2-T)**	**P(DPP2ODT2-T)**
V_{th} [V]	8 ± 8	11 ± 8
$\mu_{sat,avg}$ [cm^2/Vs][a]	0.7 ± 0.15	0.2 ± 0.03
$\mu_{sat,min}$ [cm^2/Vs][b]	0.3 ± 0.05	0.1 ± 0.01
$\mu_{sat,max}$ [cm^2/Vs][c]	1.7 ± 0.77	0.5 ± 0.12
r_{sat}[d]	0.97 ± 0.07	0.99 ± 0.06
$\mu_{sat,eff}$ [cm^2/Vs][e]	0.7 ± 0.17	0.2 ± 0.04
I_{on}/I_{off}	$1x10^5 \pm 9x10^4$	$2x10^4 \pm 1x10^4$

All numbers are averages and standard deviations of at least six devices measured in forward direction. [a] *$\mu_{sat,avg}$ are the average saturation mobilities between the threshold voltage and the maximum applied gate voltage.* [b] *$\mu_{sat,min}$ are the saturation mobilities at high gate voltages (between -60 and -80 V).* [c] *$\mu_{sat,max}$*

are the ones close to the threshold voltage (between V_{th} and V_{th} – 20 V). [d] *r_{sat} are the reliability factors and* [e] *$\mu_{sat,eff}$ the effective mobilities ($\mu_{sat,eff} = r_{sat} \cdot \mu_{sat,avg}$) suggested by Choi et al.*[33]

In order to understand the reasons behind the improved device performance of P(DPP6DOT2-T), we investigated the film structure by grazing incidence wide angle X-ray scattering (GIWAXS). **Fig. 6a** shows the 2D diffraction images of solution sheared films of P(DPP6DOT2-T) and P(DPP2ODT2-T) on ODTMS treated SiO_2. Both polymers produce multiple orders of lamellar stacking reflections and a distinct out-of-plane π-π stacking peak with P(DPP6DOT2-T) having stronger signals for comparable samples. The in-plane cuts (**Fig. 6c**) reveal that the extension of the side chains led to a decrease of the in-plane π-π stacking distance from 3.66 Å to 3.61 Å. By reducing the distance between cofacially oriented polymer backbones the overlap of the molecular HOMO orbitals (which are typically concentrated on the polymer backbone[48,49]) is increased, which has been shown to result in an improved charge transport between adjacent molecules.[23,50] The summary of the in-plane and out-of-plane π-π stacking and alkyl distances is schematically depicted in **Fig. 6b** and shows slight variations of the spacings in the different directions. From the in-plane and out-of-plane 1D plots (**Fig. 6c**) it can also be seen that not only the π-π stacking peak position is shifted for P(DPP6DOT2-T) compared to P(DPP2ODT2-T) but also that the peak is more pronounced. This indicates a larger number of domains with a larger crystalline coherence with both face-on and edge-on orientation. This overall increase in crystallinity due to the extension of the side chains is in good agreement with previous reports on spin coated blends of DPP-based polymers with fullerene.[51] We therefore believe that both the reduced π-π stacking distance and the increased structural order in the films, most likely due to the higher propensity for aggregation in solution as has already been seen from the gel permeation chromatography, are the reasons for the improved charge transport in the transistors.

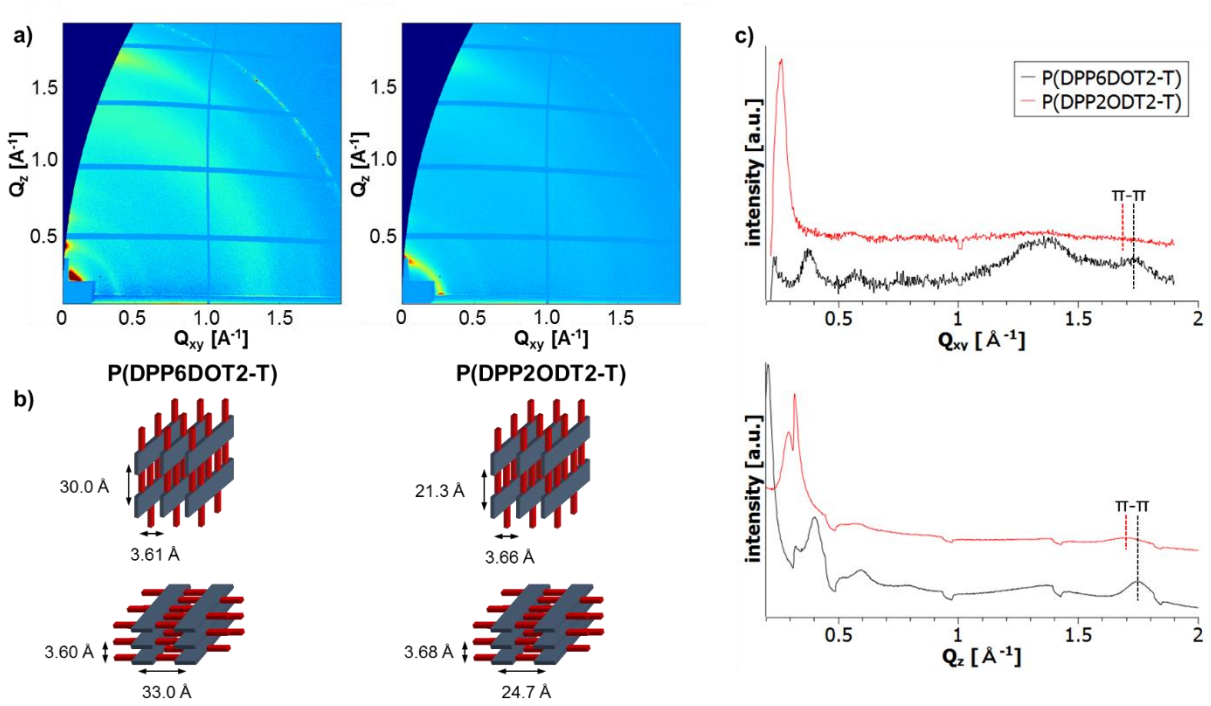

Fig. 6 *a) GIWAXS 2D images of P(DPP6DOT2-T) and P(DPP2ODT2-T). b) Schematics of the packing regimes (top: edge-on, bottom: face-on) in the solution sheared films including the various π-π and alkyl spacings. P(DPP6DOT2-T) shows a reduced π-π stacking distance and increased alkyl spacing in edge-on and face-on orientation compared to P(DPP2ODT2-T). c) 1D scattering plots for in-plane (Q_{xy}) and out-of-plane (Q_z) directions for the two polymers. The dashed lines indicate the position of the π-π stacking peaks.*

Stability of field-effect transistors

We also investigated the stability of the optimized P(DPP6DOT2-T) devices fabricated using the ODTMS SAM. The devices were characterized immediately after fabrication, subsequently stored under ambient conditions in the dark and re-measured after 4, 16, and 58 weeks (**Table S2**). Over this period, only a small decrease in on-current occurred as evident from the transfer characteristics (**Fig. 7a**). Furthermore, a reduction of the "kink" in the $I_d^{1/2}$ curves can be seen. This can be shown even more clearly when $\mu_{sat,avg}$, $\mu_{sat,max}$ and $\mu_{sat,min}$ are plotted over time (**Fig. 7b**). The graph shows that the difference between $\mu_{sat,max}$ and $\mu_{sat,min}$ is reduced over time. We attribute this effect to a decrease in contact resistance over time as has been reported for other organic semiconductors in the literature.[31,52] The transistor parameters are summarized in Table S2 and it can be seen that the average saturation mobility only decreased from 0.6 cm^2/Vs to 0.5 cm^2/Vs (reduction by 17%) after 58 weeks storage under ambient conditions,

which is a promising starting point for potential long-term stability important for device applications. Additionally, we observed an increase in off-current with storage time leading to a decrease in the on/off ratio. This behavior together with the reduction in subthreshold slope indicates that there is a doping effect over time, for example by oxygen, creating charge carriers in the semiconductor as has been observed previously for organic semiconductors.[53,54] Recently, it has been shown that this effect can be mitigated by the addition of molecular dopants (e.g. cyanocarbons or aminosilanes), either during the film formation[55] or after the fabrication,[56] potentially allowing to recover V_{on} and the subthreshold slope, which will be investigated in future work.

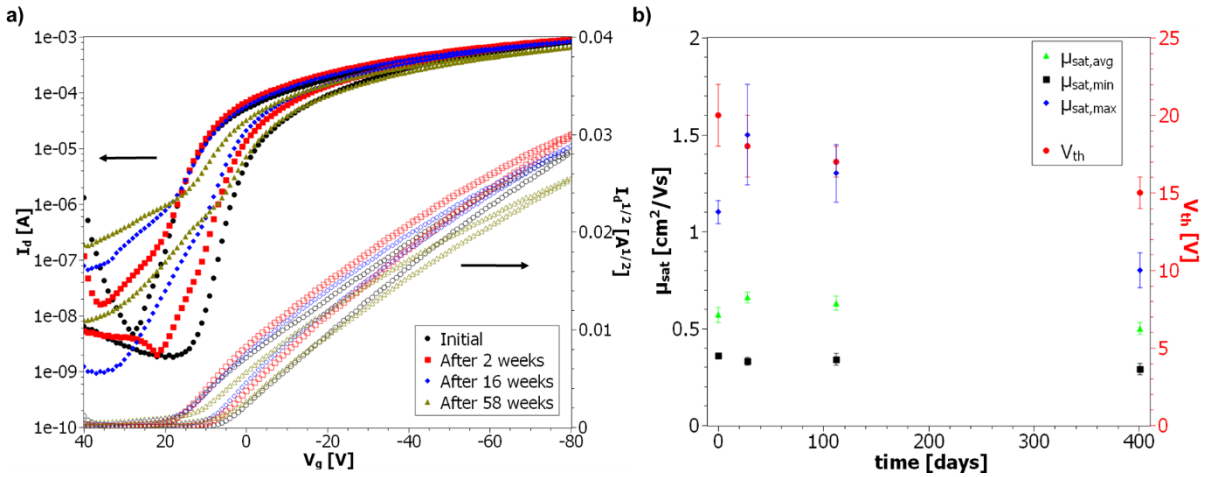

Fig. 7 *a) Transfer characteristics of solution sheared P(DPP6DOT2-T) transistors measured directly after fabrication and after 2, 16 and 58 weeks storage under ambient condition. b) Saturation mobility and threshold voltage of P(DPP6DOT2-T) transistors stored in ambient conditions measured at different times after fabrication. It can be seen that the devices are reasonably stable over more than one year of storage. The lines act as guide for the eye.*

Conclusion

In summary, we have introduced a new DPP-based polymer P(DPP6DOT2-T) with extended solubilizing side chains and branching points further away from the polymer backbone. Bottom-gate top-contact field-effect transistors with the solution sheared polymer exhibit average saturation mobilities between 0.1 – 0.8 cm^2/Vs depending on the shearing speed and the used surface-modifying SAM. By applying charge modulation spectroscopy, we were able to show

that the increased mobility for devices with ODTMS SAM can be attributed to a higher degree of polaron delocalization in the films.

The optimized OFETs using the polymer with the extended side chains and the ODTMS SAM achieved average saturation mobilities of up to 1 cm^2/Vs. This is an improvement by more than a factor of three compared to the reference devices with the polymer having the standard octyldodecyl side chains. The improved charge transport in P(DPP6DOT2-T) has been attributed to a more beneficial molecular packing in the solution sheared films due to the extended side chains. From GIWAXS we determined that the extension of the side chains produces films in which the π-π stacking distance between neighboring chains is reduced and the relative fraction of crystalline domains is increased. Both these effects likely contribute to the improvement in charge carrier transport. Finally, we showed that the devices exhibit a very promising stability under ambient conditions with only minor degradation in mobility and threshold voltage over a time span of more than a year.

Methods

Materials

All chemicals, solvents and the different silanes used as self-assembled monolayers, octadecyltrimethoxysilane (ODTMS), octyltrimethoxysilane (OTMS), and phenyltrimethoxysilane (PTMS), were purchased from Sigma Aldrich and used as received. The monomers 3,6-Bis(5-bromothiophen-2-yl)-2,5-bis(6-dodecyloctadecyl)pyrrolo[3,4-*c*]pyrrole-1,4(2*H*,5*H*)-dione (DPP6DOT2Br2) and DPP2ODT2Br2 (**Fig. S1**) were synthesized based on the procedures reported in the literature.[14,19,51]

Polymer synthesis

Under nitrogen atmosphere, DPP6DOT2Br2 (568 mg, 0.437 mmol, 1.0 eq.), 2,5-bis(trimethylstannyl)thiophene (179 mg, 0.437 mmol, 1.0 eq.), tris(dibenzylideneacetone) dipalladium(0) (8.0 mg, 8.73 µmol, 0.02 eq.) and tri(o-tolyl)phosphine (10.6 mg, 34.94 µmol, 0.08 eq.) were dissolved in anhydrous chlorobenzene and heated up to 130 °C under vigorous

stirring. After 16 h at 130 °C, the reaction mixture was allowed to cool down and hydrogen chloride methanol solution (3.4 ml, 1.25 M) was added. After stirring for 4.5 h, the reaction mixture was poured into methanol, solids were collected by filtration and subsequently purified by Soxhlet extraction using methanol, acetone and hexane. The remaining polymer material was dissolved by dichloromethane, precipitated into methanol, isolated by filtration and dried in vacuum at 40 °C overnight. A dark solid was obtained (510 mg, 96 %). ^{1}H NMR ($C_2D_2Cl_4$, 393 K, 500 MHz) δ [ppm] = 8.82 (br. s.), 7.20 (br. s.), 4.12 (br. s.), 1.75 – 1.10 (br. s.), 0.94 (br. s.) (**Fig. S10**). HT-GPC (1,2,4-TCB, 150 °C): M_n = 19.4 kg/mol, M_w = 49.2 kg/mol, Đ = 2.54. GPC ($CHCl_3$, 40 °C): M_n = 160.5 kg/mol, M_w = 378.4 kg/mol, Đ = 2.36 (**Fig. S11** and **S12**).

Instrumentation

Proton ^{1}H and carbon ^{13}C *nuclear magnetic resonance* (NMR) spectra were recorded at 500.13 MHz and 125.75 MHz, respectively, using a Bruker Avance III 500 spectrometer and the specified solvents. The NMR spectra were referenced to the residual non-deuterated solvent signals of chloroform-*d* ($CDCl_3$: $\delta(^{1}H)$ = 7.26 ppm, $\delta(^{13}C)$ = 77.16 ppm) or tetrachloroethane-d_2 ($C_2D_2Cl_4$: $\delta(^{1}H)$ = 5.98 ppm, $\delta(^{13}C)$ = 73.37 ppm). Abbreviations were used for ^{1}H NMR spectra data as listed: br. s. - broad signal.

For *gel permeation chromatography* (GPC) a PL-GPC 50 Plus (Polymer Laboratories, USA) normal-temperature size exclusion chromatograph was used comprising an UV/Vis and refractive index detector and a three-column system (pre-column ResiPore and first/second main column Resipore/PLgel 5µm Mixed-C). Measurements were performed using chloroform as eluent at 40 °C and at 1 ml/min flow rate. Sample solutions (c = 2 mg/ml) were filtered through PTFE filter (0.2 µm pore size) before the injection. Number average-molecular weights (M_n) and dispersities (Đ = M_w/M_n) were calculated based on calibration with polystyrene standards (Polymer Standards Service (PSS), Germany).

High-temperature GPC (HT-GPC) measurements were carried out on a PL-GPC 220 (Polymer Laboratories, USA) with two MIXED-B-LS columns and 1,2,4-trichlorobenzene (TCB) as eluent

at 150 °C and at 1 ml/min flow rate. Samples (2.5-3.0 mg/ml) were stirred at 150 °C for 7 h, then kept at 80 °C and heated up to 150 °C for 2 h prior to each measurement.

Thermogravimetric analysis (TGA) was conducted on a TA Instruments Q5000 applying a nitrogen gas flow and a heating rate of 10 K/min. The decomposition temperature T_d was determined at 5 % weight loss.

Differential scanning calorimetry (DSC) was performed on a TA Instruments Q1000 at a scan rate of 10 K/min under nitrogen atmosphere (**Fig. S3**).

Cyclic voltammetry (CV) was conducted using a three-electrode setup comprising a non-aqueous Ag/Ag+ reference electrode, a platinum wire as auxiliary electrode and a platinum disc working electrode on which a thin film of the polymer sample was freshly deposited prior to each measurement. Deoxygenated, anhydrous acetonitrile was used as solvent and tetra-*n*-butylammonium hexafluorophosphate (0.1 M) as electrolyte. Voltammograms were recorded at 50 mV/s and externally referenced to the signal of the ferrocene/ferrocenium redox couple. The energy of the highest occupied molecular orbital (HOMO) was calculated according to the equation E_{HOMO} = - (5.09 + $E_{onset,ox\ vs.\ Fc/Fc+}$) [eV].[19,57] The energy of the lowest unoccupied molecular orbital (LUMO) was calculated considering the band gap energy (E_g) estimated from thin-film UV/Vis absorption spectra: $E_{LUMO} = E_{HOMO} + E_g$.

UV/Vis spectroscopy was carried out using a Specord 210 Plus (Analytik Jena, Germany) at a scan rate of 20 nm/s. Thin polymer film samples were fabricated on glass slides by drop casting from chloroform (c ~ 1 mg/ml). The energy of the band gap was calculated using the onset absorption wavelength λ_{onset}^{abs} determined from the absorption edge to high wavelengths and the following equation.

$$E = \frac{h \cdot c}{\lambda} \quad \rightarrow \quad E_g \approx \frac{1240\ nm}{\lambda_{onset}^{abs}}\ [eV]$$

Device fabrication and characterization

Highly n-doped silicon wafers with 300 nm wet grown oxide (Active Business Company GmbH) were used as substrates for the OFETs. The substrates were cleaned by sequential sonication

for 10 min each in detergent, de-ionized water, acetone, and 2-propanol. After the cleaning, the substrates were blown dry by nitrogen. The different silane SAMs were deposited based on the protocol reported by Ito et al.[58] Solutions with 3 mM of ODTMS, OTMS, and PTMS in trichloroethylene were dispensed onto the cleaned substrates after they have been exposed to a UV-ozone plasma for 10 min. The solution was allowed to partially assemble for 10 s on the wafer before spin coating for 30 s at 3000 rpm. After the spin coating the substrates were stored in a vacuum desiccator together with a small amount (approximately 1 mL) of ammonium hydroxide (~30% in water) in a vial for 15 h. The substrates were then sonicated and rinsed with toluene before being blown dry with nitrogen.

P(DPP6DOT2-T) and P(DPP2ODT2-T) were dissolved in chlorobenzene at 8 mg/mL and stirred on a hot plate for 2 h at 40 °C. After dissolving the solutions were filtered through a 0.2 µm PTFE filter. Films of the polymers on the various substrates were then fabricated using a solution shearing setup.[23] The setup consists of a heated substrate plate and a moving blade. For the blade a silicon wafer piece with a hydrophobic ODTMS SAM was used. The angle between blade and substrate was 8° and the blade-substrate gap was 100 µm. The substrate was heated to 60 °C and the films were coated at speeds between 0.1 and 0.5 mm/s. To finish the devices, 50 nm gold source-drain gold electrodes were defined by thermal evaporation in vacuum. The deposition rate was around 1.5 Å/s at a chamber pressure of ~10^{-7} mbar.

The transistor characteristics were acquired with a Cascade Microtech MPS150 probe station and a Keysight B1500A Semiconductor Device Analyzer with three high resolution source monitor units. All fabrication and characterization steps were performed under ambient conditions.

Charge modulation spectroscopy

Lightly doped Silicon substrates with a 150 nm SiO_2 dielectric layer were used as the CMS substrates. The cleaning and treatment with the ODTMS SAM of the substrates was performed in the same way as for the OFET devices followed by the solution shearing of the P(DPP6DOT2-T) with the optimized coating conditions. To complete the CMS device, 15 nm

thick gold electrodes were deposited in a nitrogen glove-box using a thermal evaporator. The samples were then individually loaded into a home-built nitrogen sample chamber with KBr windows to prevent oxygen degradation while maintaining IR transmissivity during the CMS measurements.

CMS measurements were carried out as described previously[46] using a home-built FT-IR system by alternately biasing the samples at Vg = -10 V and -30 V. Since DPP-based copolymers are expected to be ambipolar, these gate voltages (Vg) were chosen to ensure that only mobile holes would be induced by field-effect and studied in our samples over the course of the entire measurement. The resulting differential infra-red spectrum (ΔT/T) in transmission, averaged more than 2,000 times, was measured using a Nicolet iS50 FT-IR in conjunction with a Keithley 2400 to give the spectra.

GIWAXS measurements

Samples for grazing incidence wide angle X-ray scattering were prepared on highly n-doped silicon wafers. The substrates were cleaned in the same way as for the devices and the films were prepared with identical processing conditions. All the measurements were performed at the SAXS beamline at Elettra in Trieste, Italy. The detector was a Dectris Pilatus 1M and the photon beam energy was 8 keV. The sample-detector distance and the beam center were determined by a silver behenate scattering standard. The grazing incidence angle for all measurements was 0.153° and the samples were exposed to the beam for 600 s. The scattering data was analyzed with WxDiff.[59]

Acknowledgements

The authors would like to acknowledge support by the German Excellence Initiative via the Cluster of Excellence EXC 1056 “Center for Advancing Electronics Dresden” (cfaed). M.H. acknowledges financial support from the Graduate Academy Dresden and the Center for Advancing Electronics Dresden. T.E. acknowledges support by the Feodor Lynen Research Fellowship of the German Humboldt Foundation. A.S. and A.R.C. acknowledge financial

support from the National Science Foundation, DMREF program, award #DMR 1533987. The authors would like to thank Rishi Shivhare for help with the GIWAXS measurements and Luigi Castriotta for help with the device characterization.

References

1 Y. N. Li, P. Sonar, L. Murphy and W. Hong, *Energy Environ. Sci.*, 2013, **6**, 1684.

2 J. Li, Y. Zhao, H. S. Tan, Y. Guo, C.-A. A. Di, G. Yu, Y. Liu, M. Lin, S. H. Lim, Y. Zhou, H. Su and B. S. Ong, *Sci. Rep.*, 2012, **2**, 754.

3 Z. Chen, M. J. Lee, R. Shahid Ashraf, Y. Gu, S. Albert-Seifried, M. Meedom Nielsen, B. Schroeder, T. D. Anthopoulos, M. Heeney, I. McCulloch and H. Sirringhaus, *Adv. Mater.*, 2012, **24**, 647–652.

4 K. H. Hendriks, G. H. L. Heintges, V. S. Gevaerts, M. M. Wienk and R. A. J. Janssen, *Angew. Chemie Int. Ed.*, 2013, **52**, 8341–8344.

5 X. Cheng, M. Caironi, Y.-Y. Noh, J. Wang, C. Newman, H. Yan, A. Facchetti and H. Sirringhaus, *Chem. Mater.*, 2010, **22**, 1559–1566.

6 Z. Yi, S. Wang and Y. Liu, *Adv. Mater.*, 2015, **27**, 3589–3606.

7 C. B. Nielsen, M. Turbiez and I. McCulloch, *Adv. Mater.*, 2013, **25**, 1859–1880.

8 A. Armin, M. Hambsch, P. Wolfer, H. Jin, J. Li, Z. Shi, P. L. Burn and P. Meredith, *Adv. Energy Mater.*, 2015, **5**, 1401221.

9 A. Armin, P. Wolfer, P. E. Shaw, M. Hambsch, F. Maasoumi, M. Ullah, E. Gann, C. R. McNeill, J. Li, Z. Shi, P. L. Burn and P. Meredith, *J. Mater. Chem. C*, 2015, **3**, 10799–10812.

10 W. Li, W. S. C. Roelofs, M. Turbiez, M. M. Wienk and R. A. J. Janssen, *Adv. Mater.*, 2014, **26**, 3304–3309.

11 M. Li, J. Li, D. Di Carlo Rasi, F. J. M. Colberts, J. Wang, G. H. L. Heintges, B. Lin, W.

Li, W. Ma, M. M. Wienk and R. A. J. Janssen, *Adv. Energy Mater.*, 2018, **1800550**, 1800550.

12 A. Armin, R. D. Jansen-Van Vuuren, N. Kopidakis, P. L. Burn and P. Meredith, *Nat. Commun.*, 2015, **6**, 1–8.

13 S. Wu, B. Xiao, B. Zhao, Z. He, H. Wu and Y. Cao, *Small*, 2016, **12**, 3374–3380.

14 R. Di Pietro, T. Erdmann, J. H. Carpenter, N. Wang, R. R. Shivhare, P. Formanek, C. Heintze, B. Voit, D. Neher, H. Ade and A. Kiriy, *Chem. Mater.*, 2017, **29**, 10220–10232.

15 J. Yao, C. Yu, Z. Liu, H. Luo, Y. Yang, G. Zhang and D. Zhang, *J. Am. Chem. Soc.*, 2016, **138**, 173–185.

16 Z. Wang, Z. Liu, L. Ning, M. Xiao, Y. Yi, Z. Cai, A. Sadhanala, G. Zhang, W. Chen, H. Sirringhaus and D. Zhang, *Chem. Mater.*, 2018, **30**, 3090–3100.

17 J. S. Lee, S. K. Son, S. Song, H. Kim, D. R. Lee, K. Kim, M. J. Ko, D. H. Choi, B. Kim and J. H. Cho, *Chem. Mater.*, 2012, **24**, 1316–1323.

18 H. Chen, Y. Guo, G. Yu, Y. Zhao, J. Zhang, D. Gao, H. Liu and Y. Liu, *Adv. Mater.*, 2012, **24**, 4618–4622.

19 Y. Karpov, T. Erdmann, I. Raguzin, M. Al-Hussein, M. Binner, U. Lappan, M. Stamm, K. L. Gerasimov, T. Beryozkina, V. Bakulev, D. V. Anokhin, D. A. Ivanov, F. Günther, S. Gemming, G. Seifert, B. Voit, R. Di Pietro and A. Kiriy, *Adv. Mater.*, 2016, **28**, 6003–6010.

20 J. C. Bijleveld, A. P. Zoombelt, S. G. J. Mathijssen, M. M. Wienk, M. Turbiez, D. M. de Leeuw and R. A. J. Janssen, *J. Am. Chem. Soc.*, 2009, **131**, 16616–16617.

21 X. Zhang, L. J. Richter, D. M. DeLongchamp, R. J. Kline, M. R. Hammond, I. McCulloch, M. Heeney, R. S. Ashraf, J. N. Smith, T. D. Anthopoulos, B. Schroeder, Y. H. Geerts, D. A. Fischer and M. F. Toney, *J. Am. Chem. Soc.*, 2011, **133**, 15073–15084.

22 G. B. Yoon, H.-Y. Kwon, S.-H. Jung, J. J.-K. J. J.-K. Lee and J. J.-K. J. J.-K. Lee, *ACS Appl. Mater. Interfaces*, 2017, **9**, 39502–39510.

23 G. Giri, E. Verploegen, S. C. B. Mannsfeld, S. Atahan-Evrenk, D. H. Kim, S. Y. Lee, H. Becerril, A. Aspuru-Guzik, M. F. Toney and Z. Bao, *Nature*, 2011, **480**, 504–508.

24 K. Haase, C. Teixeira da Rocha, C. Hauenstein, Y. Zheng, M. Hambsch and S. C. B. Mannsfeld, *Adv. Electron. Mater.*, 2018, **4**, 1800076.

25 C. Teixeira da Rocha, K. Haase, Y. Zheng, M. Löffler, M. Hambsch and S. C. B. Mannsfeld, *Adv. Electron. Mater.*, 2018, **4**, 1800141.

26 F. Zhang, E. Mohammadi, X. Luo, J. Strzalka, J. Mei and Y. Diao, *Langmuir*, 2018, **34**, 1109–1122.

27 G. Qu, X. Zhao, G. M. Newbloom, F. Zhang, E. Mohammadi, J. W. Strzalka, L. D. Pozzo, J. Mei and Y. Diao, *ACS Appl. Mater. Interfaces*, 2017, **9**, 27863–27874.

28 S. Schott, E. Gann, L. Thomsen, S.-H. H. Jung, J. K. Lee, C. R. McNeill and H. Sirringhaus, *Adv. Mater.*, 2015, **27**, 7356–7364.

29 D. Braga and G. Horowitz, *Adv. Mater.*, 2009, **21**, 1473–1486.

30 T. Uemura, C. Rolin, T.-H. H. Ke, P. Fesenko, J. Genoe, P. Heremans and J. Takeya, *Adv. Mater.*, 2016, **28**, 151–155.

31 E. G. Bittle, J. I. Basham, T. N. Jackson, O. D. Jurchescu and D. J. Gundlach, *Nat. Commun.*, 2016, **7**, 10908.

32 I. McCulloch, A. Salleo and M. Chabinyc, *Science (80-.).*, 2016, **352**, 1521–1522.

33 H. H. Choi, K. Cho, C. D. Frisbie, H. Sirringhaus and V. Podzorov, *Nat. Mater.*, 2017, **17**, 2–7.

34 A. F. Paterson, S. Singh, K. J. Fallon, T. Hodsden, Y. Han, B. C. Schroeder, H. Bronstein, M. Heeney, I. McCulloch and T. D. Anthopoulos, *Adv. Mater.*, 2018, **1801079**, 1801079.

35 E. Mohammadi, C. Zhao, Y. Meng, G. Qu, F. Zhang, X. Zhao, J. Mei, J.-M. M. Zuo, D. Shukla and Y. Diao, *Nat. Commun.*, 2017, **8**, 16070.

36 S. K. Samanta, I. Song, J. H. Yoo and J. H. Oh, *ACS Appl. Mater. Interfaces*, 2018, **10**, 32444–32453.

37 G. Qu, J. J. Kwok, E. Mohammadi, F. Zhang and Y. Diao, *ACS Appl. Mater. Interfaces*, 2018, **10**, 40692–40701.

38 S. Kobayashi, T. Nishikawa, T. Takenobu, S. Mori, T. Shimoda, T. Mitani, H. Shimotani, N. Yoshimoto, S. Ogawa and Y. Iwasa, *Nat. Mater.*, 2004, **3**, 317–322.

39 K. P. Pernstich, S. Haas, D. Oberhoff, C. Goldmann, D. J. Gundlach, B. Batlogg, A. N. Rashid and G. Schitter, *J. Appl. Phys.*, 2004, **96**, 6431–6438.

40 P. J. Brown, H. Sirringhaus, M. Harrison, M. Shkunov and R. H. Friend, *Phys. Rev. B*, 2001, **63**, 125204.

41 D. Beljonne, J. Cornil, H. Sirringhaus, P. J. Brown, M. Shkunov, R. H. Friend and J. L. Brédas, *Adv. Funct. Mater.*, 2001, **11**, 229–234.

42 N. Zhao, Y. Y. Noh, J. F. Chang, M. Heeney, I. McCulloch and H. Sirringhaus, *Adv. Mater.*, 2009, **21**, 3759–3763.

43 V. Coropceanu, J. Cornil, D. A. da Silva Filho, Y. Olivier, R. Silbey and J.-L. Brédas, *Chem. Rev.*, 2007, **107**, 926–952.

44 H. Sirringhaus, P. J. Brown, R. H. Friend, M. M. Nielsen, K. Bechgaard, B. M. W. Langeveld-Voss, A. J. H. Spiering, R. A. J. Janssen, E. W. Meijer, P. Herwig and D. M. de Leeuw, *Nature*, 1999, **401**, 685–688.

45 R. Ghosh, C. M. Pochas and F. C. Spano, *J. Phys. Chem. C*, 2016, **120**, 11394–11406.

46 A. R. Chew, R. Ghosh, V. Pakhnyuk, J. Onorato, E. C. Davidson, R. A. Segalman, C. K. Luscombe, F. C. Spano and A. Salleo, *Adv. Funct. Mater.*, 2018, **28**, 1804142.

47 F. Liu, C. Wang, J. K. Baral, L. Zhang, J. J. Watkins, A. L. Briseno and T. P. Russell, *J. Am. Chem. Soc.*, 2013, **135**, 19248–19259.

48 H. Bronstein, E. Collado-Fregoso, A. Hadipour, Y. W. Soon, Z. Huang, S. D. Dimitrov, R. S. Ashraf, B. P. Rand, S. E. Watkins, P. S. Tuladhar, I. Meager, J. R. Durrant and I. McCulloch, *Adv. Funct. Mater.*, 2013, **23**, 5647–5654.

49 A. J. Kronemeijer, E. Gili, M. Shahid, J. Rivnay, A. Salleo, M. Heeney and H. Sirringhaus, *Adv. Mater.*, 2012, **24**, 1558–1565.

50 J. L. Bredas, J. P. Calbert, D. A. da Silva Filho and J. Cornil, *Proc. Natl. Acad. Sci.*, 2002, **99**, 5804–5809.

51 R. Shivhare, T. Erdmann, U. Hörmann, E. Collado-Fregoso, S. Zeiske, J. Benduhn, S. Ullbrich, R. Hübner, M. Hambsch, A. Kiriy, B. Voit, D. Neher, K. Vandewal and S. C. B. Mannsfeld, *Chem. Mater.*, 2018, **30**, 6801–6809.

52 C. Liu, G. Li, R. Di Pietro, J. Huang, Y.-Y. Noh, X. Liu and T. Minari, *Phys. Rev. Appl.*, 2017, **8**, 034020.

53 M. S. A. Abdou, F. P. Orfino, Y. Son and S. Holdcroft, *J. Am. Chem. Soc.*, 1997, **119**, 4518–4524.

54 E. J. Meijer, C. Detcheverry, P. J. Baesjou, E. van Veenendaal, D. M. de Leeuw and T. M. Klapwijk, *J. Appl. Phys.*, 2003, **93**, 4831–4835.

55 V. Pecunia, M. Nikolka, A. Sou, I. Nasrallah, A. Y. Amin, I. McCulloch and H. Sirringhaus, *Adv. Mater.*, 2017, **29**, 1606938.

56 N. Shin, J. Zessin, M. H. Lee, M. Hambsch and S. C. B. Mannsfeld, *Adv. Funct. Mater.*, 2018, **28**, 1802265.

57 C. M. Cardona, W. Li, A. E. Kaifer, D. Stockdale and G. C. Bazan, *Adv. Mater.*, 2011, **23**, 2367–2371.

58 Y. Ito, A. A. Virkar, S. Mannsfeld, J. H. Oh, M. Toney, J. Locklin and Z. Bao, *J. Am. Chem. Soc.*, 2009, **131**, 9396–9404.

59 Q. Yuan, S. C. B. Mannsfeld, M. L. Tang, M. F. Toney, J. Lüning and Z. Bao, *J. Am. Chem. Soc.*, 2008, **130**, 3502–3508.

Table of Contents Entry

Side chain extension leads to improved charge carrier mobility in diketopyrrolopyrrole-based donor-acceptor copolymers.